Space Weather

RESEARCH ARTICLE
10.1029/2023SW003818

Influences of Space Weather Forecasting Uncertainty on Satellite Conjunction Assessment

William E. Parker[1], Mervyn Freeman[2], Gareth Chisham[2], Andrew Kavanagh[2], Peng Mun Siew[1], Victor Rodriguez-Fernandez[3], and Richard Linares[1]

[1]Massachusetts Institute of Technology, Cambridge, MA, UK, [2]British Antarctic Survey, Cambridge, UK, [3]Universidad Politécnica de Madrid, Madrid, Spain

Key Points:

- Poor forecasts of space weather drivers inhibit our ability to perform actionable satellite conjunction assessment with advance notice
- Climatology-based probabilistic forecasts are developed for $F_{10.7}$ and K_p, which are used to assess satellite conjunction scenarios
- Providing probabilistic forecasts of the space weather drivers makes a meaningful difference in maneuver decision-making

Correspondence to:
W. E. Parker,
wparker@mit.edu

Citation:
Parker, W. E., Freeman, M., Chisham, G., Kavanagh, A., Mun Siew, P., Rodriguez-Fernandez, V., & Linares, R. (2024). Influences of space weather forecasting uncertainty on satellite conjunction assessment. *Space Weather*, *22*, e2023SW003818. https://doi.org/10.1029/2023SW003818

Received 1 DEC 2023
Accepted 8 JUL 2024

Author Contributions:
Conceptualization: William E. Parker
Formal analysis: William E. Parker
Funding acquisition: William E. Parker
Investigation: William E. Parker
Methodology: William E. Parker, Mervyn Freeman, Gareth Chisham, Andrew Kavanagh
Software: William E. Parker
Supervision: Mervyn Freeman, Gareth Chisham, Andrew Kavanagh, Peng Mun Siew, Victor Rodriguez-Fernandez, Richard Linares
Visualization: William E. Parker
Writing – original draft: William E. Parker
Writing – review & editing: William E. Parker, Mervyn Freeman, Gareth Chisham, Andrew Kavanagh, Peng Mun Siew, Victor Rodriguez-Fernandez, Richard Linares

Abstract A significant increase in the number of anthropogenic objects in Earth orbit has necessitated the development of satellite conjunction assessment and collision avoidance capabilities for new spacecraft. Neutral mass density variability in the thermosphere, driven by enhanced geomagnetic activity and solar EUV absorption, is a major source of satellite propagation error. This work investigates the impacts of space weather driver forecasting uncertainty on satellite drag and collision avoidance maneuver decision-making. Since most operational space weather driver forecasts do not offer an uncertainty assessment, the satellite operator community is left to make dangerous assumptions about the trustworthiness of the forecast models they use to perform satellite state propagation. Climatological persistence-based forecast models are developed for $F_{10.7}$ and *Kp*. These models accurately capture the heteroscedastic and, at times, highly non-Gaussian uncertainty distribution on forecasts of the drivers of interest. A set of realistic satellite conjunction scenarios is simulated to demonstrate the contributions of space weather driver forecast uncertainty on the probability of collision and maneuver decisions. Improved driver forecasts, especially forecasts of $F_{10.7}$, are demonstrated to be very useful for enabling durable maneuver decisions with additional lead time (up to 24 hr for the period examined), though the improvement depends on the specific conjunction scenario of interest.

Plain Language Summary As low earth orbit has become crowded with new satellites and debris, operators have been forced to maneuver satellites to avoid collisions on a regular basis. The drag force on a satellite, which can significantly affect the orbital path, varies depending on solar and geomagnetic activity. Unfortunately, solar activity and resulting impacts at Earth are difficult to predict even just a few days in advance. This paper traces space weather forecasting ability directly to impacts on satellite maneuver decision-making and finds that forecast uncertainty plays a critical role in making durable maneuver decisions.

1. Introduction

Recent rapid growth in the population of active satellites and debris objects in low Earth orbit (LEO) has led to a clear need for satellite conjunction assessment (CA), and collision avoidance (COLA) maneuvering capability. Today, a space domain awareness ecosystem exists that allows satellite operators to track objects in orbit, predict conjunctions in advance, and make decisions regarding satellite maneuvering to mitigate the risk of a collision. Organizations like the US Space Force's eighteenth and nineteenth Space Defense Squadrons provide conjunction data messages (CDMs) to operators responsible for performing the subsequent risk analysis and making COLA decisions for their assets.

With the advent of proliferated LEO constellations in recent years, CA tasks are routinely becoming more automated to reduce operator burden. Considering this growing automation of CA and COLA tasks, many operators have developed internal protocols for determining whether a COLA maneuver is appropriate for a conjunction scenario of interest. Most maneuver decisions consider the probability of collision (*Pc*), computed based on imperfect knowledge of the scenario and a model for evolving the states of the objects of interest. While the interpretation of potential conjunction events is probabilistic based on imperfect measurements and models, the potential collision event itself is deterministic. Given perfect observations and a perfect process model, the probability of collision at any time before the conjunction event should be either zero or one. However, uncertainty in measurements and satellite propagation complicates the analysis. As the time until the conjunction event wanes, better knowledge of the state of each object from new observations, along with a lower process model error, results in a better understanding of the likely outcome.

Most potential conjunction events are identified during screening about 7 days in advance of the time of closest approach (TCA) (M. Hejduk & Pachura, 2017; George & Harvey, 2011). However, many operators choose to wait until 12–24 hr or less before TCA to decide whether or not to maneuver (Krage, 2023; Moomey et al., 2023). This waiting is necessary because there is often significant process error in the state propagation of the objects involved in the conjunction. Updating the states of the objects with recent measurements constrains the growth of this process error.

Operators choose to wait to make maneuver decisions because collision avoidance maneuvers are costly. While the amount of propellant expended for collision avoidance maneuvers is typically small compared to the amount used for station-keeping, such maneuvers can routinely prevent a satellite from performing its desired task (Earth observation, serving users, charging solar panels, communicating with ground stations, etc.) for hours on end. However, many active satellites (especially small satellites) lack propulsion systems capable of performing last-minute COLA maneuvers. Instead, these satellites may often use differential-drag techniques, which can mitigate risk but require several days' notice to be effective. Even for satellites with propulsion systems, it is often inconvenient or impossible to maneuver at a moment's notice since this likely means missed passes of ground targets or lost communications opportunities. For tracked, non-maneuverable debris objects, laser-nudging may soon be an effective means of collision avoidance maneuvering (NASA, 2023), but even if this approach is implemented, it would still require advance notice exceeding the current standard for operations.

A key challenge in space domain awareness focuses on improving *covariance realism*, or making sure that the predicted uncertainty in satellite state aligns the measured errors. If satellite state propagation accuracy and uncertainty are improved, good maneuver decisions could be made sooner with the same level of risk. The following sections discuss limitations in our ability to predict satellite motion in LEO, how these limitations impact the conjunction risk assessment process, and what steps can be taken to make durable collision avoidance maneuver decisions sooner. After a discussion of the uncertainties involved in predicting satellite drag in Section 2, capabilities and limitations in forecasting atmospheric neutral mass density are discussed in Section 3. Then, the probability of collision metric is introduced and a dangerous scenario is highlighted using actual historical CDM data in Section 4. Finally, a climatological persistence-based heteroscedastic forecast model is developed for $F_{10.7}$ and *Kp*. Conjunction assessment scenarios for true collision events are simulated in Section 6. Semi-analytical and numerical methods for translating space weather driver uncertainty into satellite state uncertainty are detailed in the Appendix A.

2. Satellite Drag

As the largest contributor to state propagation error in LEO, significant effort has been devoted to improving satellite drag models in recent years. The acceleration due to atmospheric drag on a satellite is computed by

$$\ddot{\mathbf{r}}_D = -\frac{1}{2}\frac{C_d A}{m}\rho v_{rel}^2 \mathbf{e}_{rel}, \tag{1}$$

where $\mathbf{r}$ is the satellite position vector in an Earth-centered inertial frame, ρ is the atmospheric neutral mass density, v_{rel} is the magnitude of the velocity of the satellite relative to the motion of the atmosphere, C_d is the drag coefficient, A is the frontal area of the satellite normal to the direction of motion relative to the atmosphere, m is the mass of the satellite, and $\mathbf{e}_{rel}$ is the unit vector in the direction of satellite relative velocity. In practice, the uncertain C_d, A, and m are often combined as

$$B = \frac{C_d A}{m}, \tag{2}$$

or, in some cases

$$B^* = \frac{C_d A \rho_0}{2m}, \tag{3}$$

where ρ_0 is the reference density of 0.15,696,615 kg/(m$^2 \cdot R_E$), and R_E is the average Earth radius (Hoots, 1980). It follows that

$$\ddot{\mathbf{r}}_D = -\frac{1}{2}\rho v_{rel}^2 B \mathbf{e}_{rel} = -\frac{\rho}{\rho_0} v_{rel}^2 B^* \mathbf{e}_{rel}. \quad (4)$$

To accurately predict satellite drag acceleration $\ddot{\mathbf{r}}_D$(and evolve uncertainty in that prediction), it is prudent to consider each term in Equation 1 as uncertain. v_{rel} and $\mathbf{e}_{rel}$ are often well characterized during quiet periods because the winds in the upper atmosphere are much smaller in magnitude than the spacecraft's velocity. However, geomagnetic activity disturbances have been shown to produce enhanced neutral winds in the upper atmosphere. The speed of the neutral winds can, at times, approach 1 km/s, which can cause rapid unpredictable fluctuations in apparent velocity for a LEO satellite (Wang et al., 2008; Zhang & Shepherd, 2000). Mass m, exposed frontal area A, and drag coefficient C_d are often very uncertain because these quantities require knowledge of the properties of the object being tracked that cannot be readily estimated directly from remote measurements. The rough size and mass of the object under study have been inferred from past orbital history (Gondelach et al., 2017), measurements of radar cross section (Dickey & Culp, 1989) or visual magnitude (Šilha, 2020). A and C_d are a function of satellite attitude, which is difficult to measure in real-time. Still, light curve measurements have been used to better characterize the attitude dynamics for tumbling objects of interest (Linares et al., 2014; Schildknecht et al., 2017; Šilha et al., 2018). This knowledge of satellite attitude dynamics can be helpful for understanding and predicting how C_d and A vary in time. However, most previous efforts at improving drag models have focused on estimating the combined term B or B^* instead of inferring each parameter individually (Bowman, 2002; Gondelach et al., 2017; Saunders et al., 2012).

In an analysis of satellite drag forecasting error during 1 month of observations, M. D. Hejduk and Snow (2018) found that uncertainty in atmospheric density outweighed uncertainty in B 92% of the time for the population of satellites considered in their study. Variability in neutral mass density is common on both long and short timescales due to solar EUV radiation and Joule heating, respectively. Because satellite decay is so strongly influenced by solar and geomagnetic activity, significant effort has been devoted to developing improved space weather models and observation techniques to reduce the uncertainty that arises due to this extreme variability in neutral mass density.

Error in density forecasts can be attributed to either error in the predicted space weather model inputs or error in the models themselves. When focusing on errors in the space weather inputs, Bussy-Virat et al. (2018) found that accounting for uncertainties in projected $F10.7$ and A_p in the per-object covariances at TCA can lead to significantly different estimates of Pc. When considering error in the neutral mass density models, Hejduk and Snow (M. D. Hejduk & Snow, 2018) found that ignoring model uncertainty can cause dangerous conjunction events to go unnoticed, since it makes operators overly confident in potentially poor satellite state propagations. Gondelach et al. (2022) also quantified and propagated model uncertainty, but included a correlation factor between the position uncertainties of the two objects involved in the conjunction. This correlation recognizes the idea that, often, both objects involved in a conjunction will travel through similar perturbed regions of the atmosphere. In general, the goal of all of this work in uncertainty quantification is to accurately represent the true uncertainty in the predicted state of the objects being tracked based on the information available at the time of the estimate. This covariance-realism effort ensures that maneuver decisions are made based on accurate projected uncertainties, and is of much interest to the space surveillance and tracking community (Aristoff et al., 2016).

One factor that makes covariance realism difficult in operations is a lack of transparency and accessibility from both the atmospheric modeling and space weather forecasting fronts. The atmospheric model most commonly used by the United States Space Force for propagating tracked objects and creating conjunction data messages is HASDM (High-Accuracy Satellite Drag Model) (Storz et al., 2005). HASDM has the benefit of being operationally calibrated using tracked reference objects and, as a result, provides very good estimates of mass density in LEO. However, the density predictions from the model are not available to the vast majority of operators, which leaves them to use other models (usually empirically derived) for their analysis on possible mitigation actions. NRLMSISE-00 (Picone et al., 2002), NRLMSISE-2.0 (J. T. Emmert et al., 2021), DTM (Bruinsma, 2015), and JB2008 (Bowman et al., 2008) are popular choices. Some of these models (including JB2008) use space weather drivers with forecasts that are not freely available to the public. The disconnect between the operational model used to create CDMs and the analysis models used to determine mitigation actions creates dangerous and avoidable complexity in the collision avoidance decision-making process.

10.1029/2023SW003818

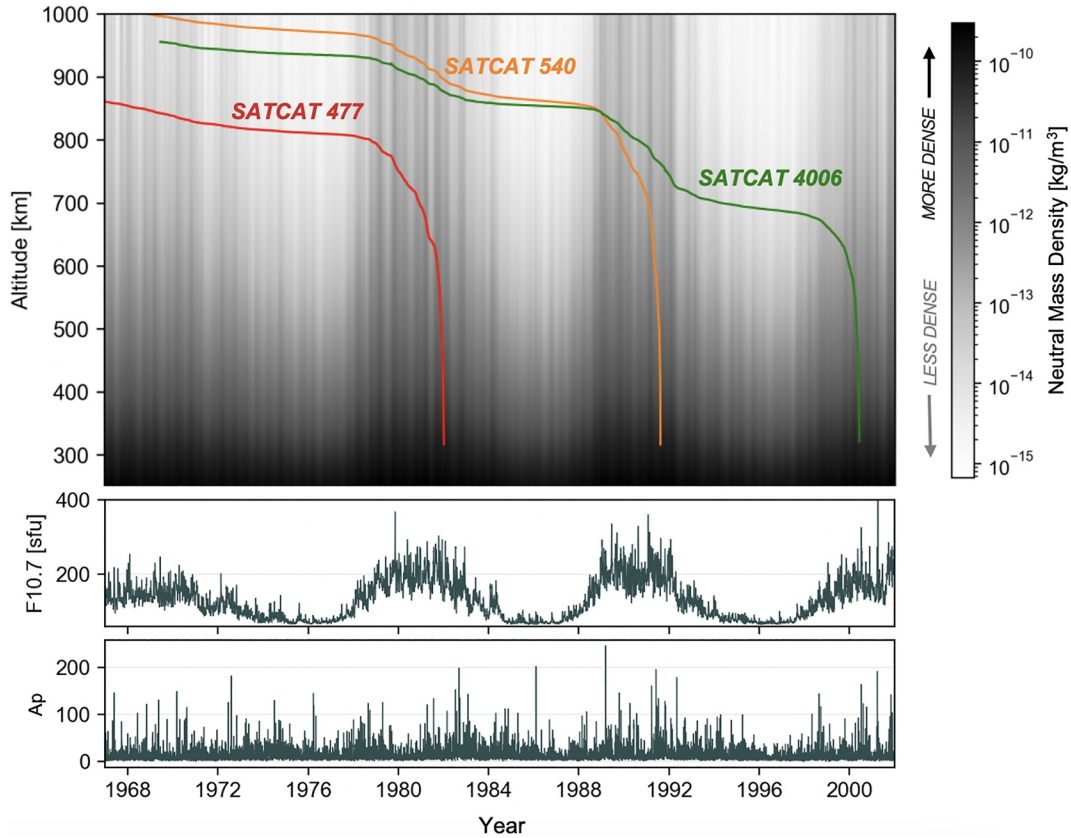

Figure 1. Passive altitude decay of SATCAT 477, 540, and 4,006 (Thor Ablestar Debris) through multiple solar cycles with globally averaged neutral mass density shown in the background for reference. Altitudes are time-averaged over one orbit. Below, a history of $F_{10.7}$ and Ap are correlated with the density trends observed over time.

3. Forecasting Neutral Mass Density

Variability in neutral density within the thermosphere is driven largely by the absorption of solar radiation in the XUV, EUV, and FUV ranges as well as Joule heating and particle precipitation during periods of enhanced geomagnetic activity. Solar UV flux drives order-of-magnitude changes in mass density over a period of years with variability in the solar cycle. Geomagnetic activity enhancements, however, can cause unpredictable changes in mass density of similar scale on the order of hours. Many models of the upper atmosphere rely on space weather indices and proxies, collectively referred to as space weather *drivers* as inputs to describe these dynamics. The drivers help to simplify complex information about the solar or geospace environment into a set of scalar variables.

One space weather driver of particular interest is $F_{10.7}$, the daily solar radio flux at 10.7 cm, which is generally a good proxy for solar EUV flux (Covington, 1948; Picone et al., 2002; Tapping, 2013). The 81-day average of the proxy, $F_{10.7A}$, is also sometimes used as an input for models. A major geomagnetic index of interest is *Kp*, a 3-hr index which is computed by combining measurements of Earth's magnetic field from 13 specific observatories around the world (Bartels, 1949). The 3-hr *Kp* index is often converted to a linear-scaled alternative called *ap*. The *Ap* index is the daily average value of *ap*. Each of these indices measures geomagnetic activity, but all three are used regularly for various reasons. Another important geomagnetic index is *Dst*, the storm-time disturbance index, which measures ring current geomagnetic activity from observatories closer to the magnetic equator. It offers 1-minute temporal resolution, compared to three-hours for *Kp*. These geomagnetic indices together help to estimate the rapid enhancements in neutral density in the thermosphere associated with Joule heating and particle precipitation that accompany geomagnetic activity enhancements.

Figure 1 shows the passive orbital decay of SATCAT 477, 540, and 4,006, three debris fragments from the Thor-Ablestar breakup event of 1,961. The background of the figure shows the historical globally averaged neutral

mass density derived from ground-based radar tracking of objects (J. Emmert et al., 2021), resolved in time and altitude. The history of satellite time-averaged altitude was extracted from two-line element (TLE) tracking data for the objects of interest. The satellite paths clearly show higher rates of decay during solar maximum (high $F_{10.7}$) than during solar minimum (low $F_{10.7}$). Small deviations in decay rate, mostly visible during solar maximum, are from rapid density enhancements caused by increased geomagnetic activity. Even though SATCAT 540 starts at a higher altitude than SATCAT 4006, it deorbits faster because it has a larger ballistic coefficient.

Several empirical and physics-based models for the dynamics of the thermosphere-ionosphere system have been developed over the years. Recent in situ measurements of thermosphere mass density from satellite missions like CHAMP (Reigber et al., 1999), GRACE (Davis et al., 2000), and Swarm (Doornbos et al., 2009) have provided excellent, while sparse, observations useful for refining atmospheric models. While significant progress has been made in modeling the response of the neutral thermosphere to enhanced geomagnetic activity, forecasts of the space weather drivers that drive the models have not been comparably improved. These poor forecasts of the space weather drivers can at times be the dominant source of uncertainty in predicting satellite drag.

Recent work in (Licata et al., 2020) benchmarked the performance of operational forecasting models for key space weather drivers like $F_{10.7}$ and *Ap*, among others. Such forecasts are typically driven by a combination of historical trends in the driver under study and a set of current related observations at the forecast time. *Recurrence* and *persistence* are two important principles for these forecasts. Recurrence considers previous observations at interval solar rotations backward in time, while persistence uses the last known value as the best guess for future values of the driver. $F_{10.7}$ forecasts can be improved beyond the recurrence or persistence models by supplementing EUV radiation observations from the east limb of the sun or a modeled nowcast of the Sun's surface magnetic field (Henney et al., 2012, 2015; Lean et al., 2009).

Forecasts of geomagnetic indices like *Kp* and its derived *ap* are typically driven by a combination of solar wind measurements at the L1 Lagrange point and a history of measurements for the index. Since measurements of solar wind at L1 provide very little advance notice of what is to arrive at Earth, forecasts of these indices typically have a short useful horizon time. Shprits et al. (2019) found that forecasts for *Kp* are only reliably accurate for a time horizon of 6–20 hr, depending on the solar cycle. Beyond 1–2 days out, forecasts based on recurrence or persistence generally produce the best results (though performance is still quite poor). The skill of a forecast model can be represented by

$$skill = 1 - \frac{RMSE}{\sigma_x}, \tag{5}$$

where, considering N samples with true values $\mathbf{x}$, estimated values $\hat{\mathbf{x}}$, and true mean μ,

$$RMSE = \sqrt{\frac{\Sigma_{i=1}^{N}(x_i - \hat{x}_i)^2}{N}} \tag{6}$$

and

$$\sigma_x = \sqrt{\frac{\Sigma_{i=1}^{N}(x_i - \mu)^2}{N}}. \tag{7}$$

A skill score of 1 corresponds to a perfect forecast and 0 corresponds to a forecast where the RMSE is equal to the standard deviation of the observations. The skill can also be negative if the error in the forecast is larger than the variability in the data it's trying to predict. A good forecast should have a skill score as high as possible.

Figure 2 shows the RMSE and skill of the NOAA Space Weather Prediction Center (SWPC) $F_{10.7}$ and *Ap* forecasts as a function of time (using a 5-year rolling average to reduce noise and make general trends apparent). These forecast models were developed in 2014 and then verified on historical data from 1986 to 2013) (NOAA Space Weather Prediction Center, n.d.). Similar verification effort has been applied to forecast models for other space weather agencies (Paouris et al., 2021). The forecasts are separated by their time horizon from 1 to 7 days, and a plot of the monthly average sunspot number is overlaid on each. Starting with $F_{10.7}$ forecasts in (a) and (b),

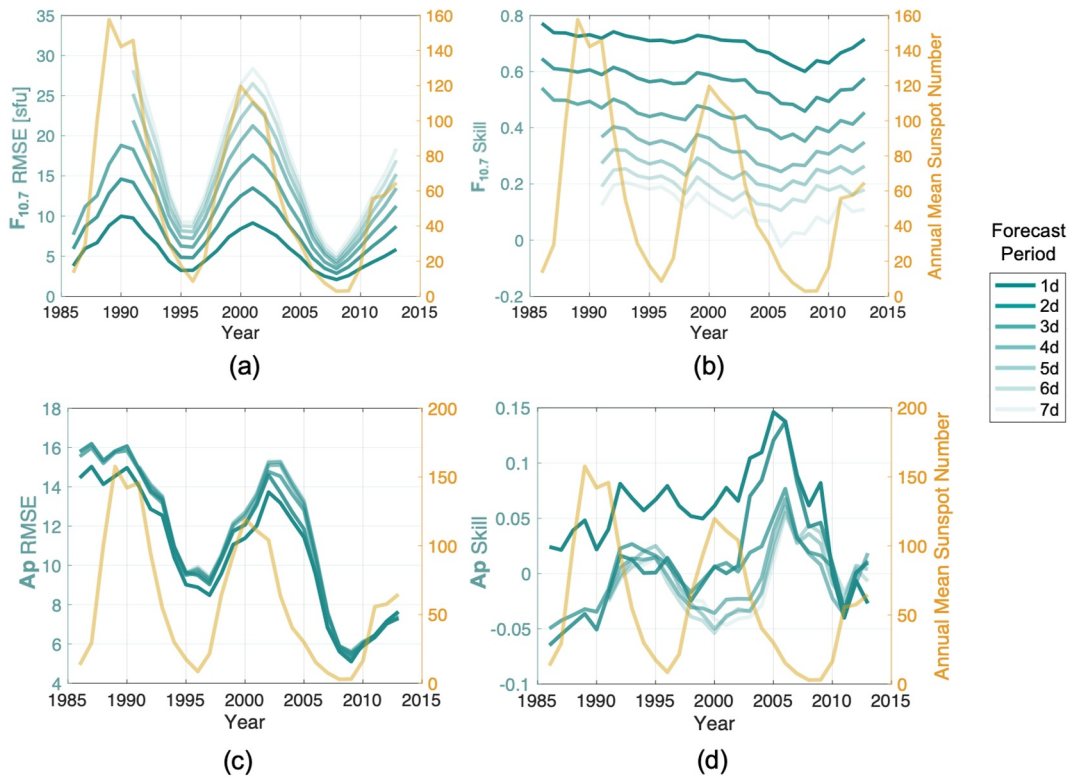

Figure 2. Forecast quality varies with the solar cycle and the desired time horizon. (a) and (b) show the 5-year rolling average of RMSE and skill, respectively, for NOAA SWPC's forecasts of $F_{10.7}$ (from 2014 model verification). (c) and (d) show a 5-year rolling average of RMSE and skill for Ap. Forecasts of $F_{10.7}$ exhibit greater skill than those for Ap. The skill of the $F_{10.7}$ forecast is relatively constant since the variability of the proxy is much larger during solar maximum than during solar minimum.

there is a clear correlation between RMSE and the solar cycle. The lowest RMSE is achieved during solar minimum. In all cases, RMSE is generally low when the forecast horizon is small, but then grows steadily with forecast time. The skill of the $F_{10.7}$ forecast appears relatively constant over time (for a forecast time horizon of interest). This is because solar radio flux exhibits much more natural variability during solar maximum, so the increased RMSE is counterbalanced by the increased variability in the true values being estimated.

The *Ap* forecasts (c) and (d) show similar correlation with the solar cycle. Increasing the forecast time horizon does not seem to change the RMSE or skill considerably, though. On close inspection, it appears that the maximum in forecast skill occurs during the declining phase of the previous solar maximum. This improvement in geomagnetic index forecasting may be attributable to the elevated coherence in the interplanetary magnetic field (IMF) that generally occurs during this decline in the solar cycle. It is unfortunate that both the $F_{10.7}$ and *Ap* forecasts struggle during solar maximum since that is the period when neutral mass density is large enough in the most populated regions of LEO for geomagnetic or solar density enhancements to have a considerable impact on satellite drag.

Figure 3 shows the deviations in *ap* and $F_{10.7}$ from truth using a simple persistence-based 1-day forecast over all recorded history for the drivers from 1957 to 2023 from the Hemholtz center at GFZ Potsdam. Figure 3a shows that *ap* forecasts are very much *heteroscedastic* with respect to the mean forecast. A heteroscedastic forecast has a variance that is dependent on the start value, the time horizon, or both. Both the mean and the distribution of the forecast variance are clearly a function of the expected value of *ap*, with very skewed distributions around low forecasted values of *ap*. Figure 3b shows that the $F_{10.7}$ forecast is also heteroscedastic (though less so than *ap*).

Figure 4 complicates this scenario further. It shows NRLMSISE-00 modeled density as a function of the input drivers, where we assume that uncertainty distributions on the drivers are Gaussian (even though Figure 3 shows that this is often not a valid assumption). 4(a) shows densities computed with input $F_{10.7} = 120$, $F_{10.7A} = 120$, and

10.1029/2023SW003818

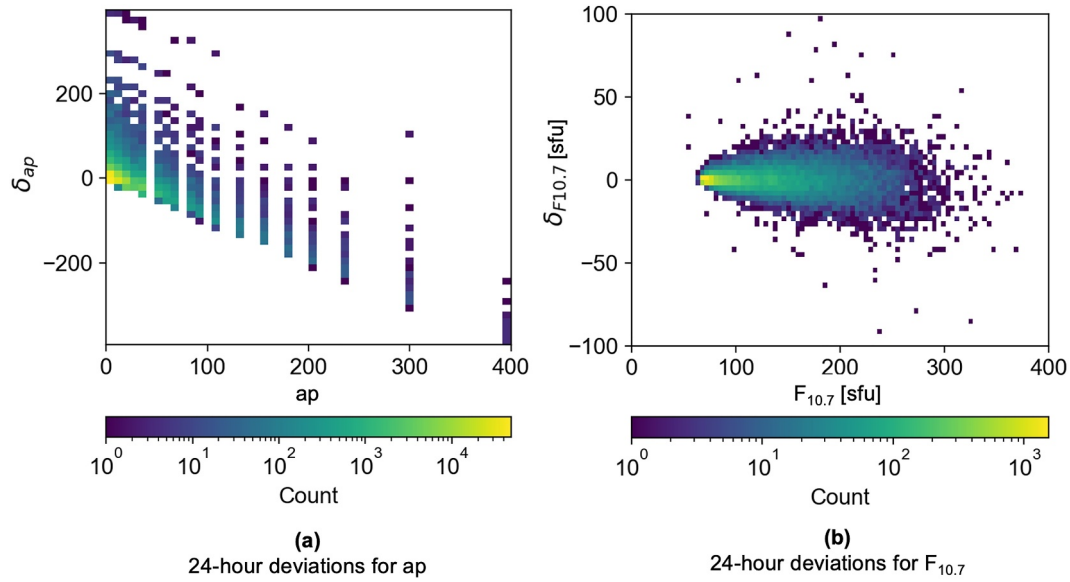

Figure 3. Deviation from 1-day forecasted drivers based on a simple persistence model using the historical record. (a) Shows the deviation in the three-hour *ap* (which has gaps because discrete values of *ap* are mapped from *Kp*), and (b) shows the deviation in the daily adjusted $F_{10.7}$. Both are heteroscedastic.

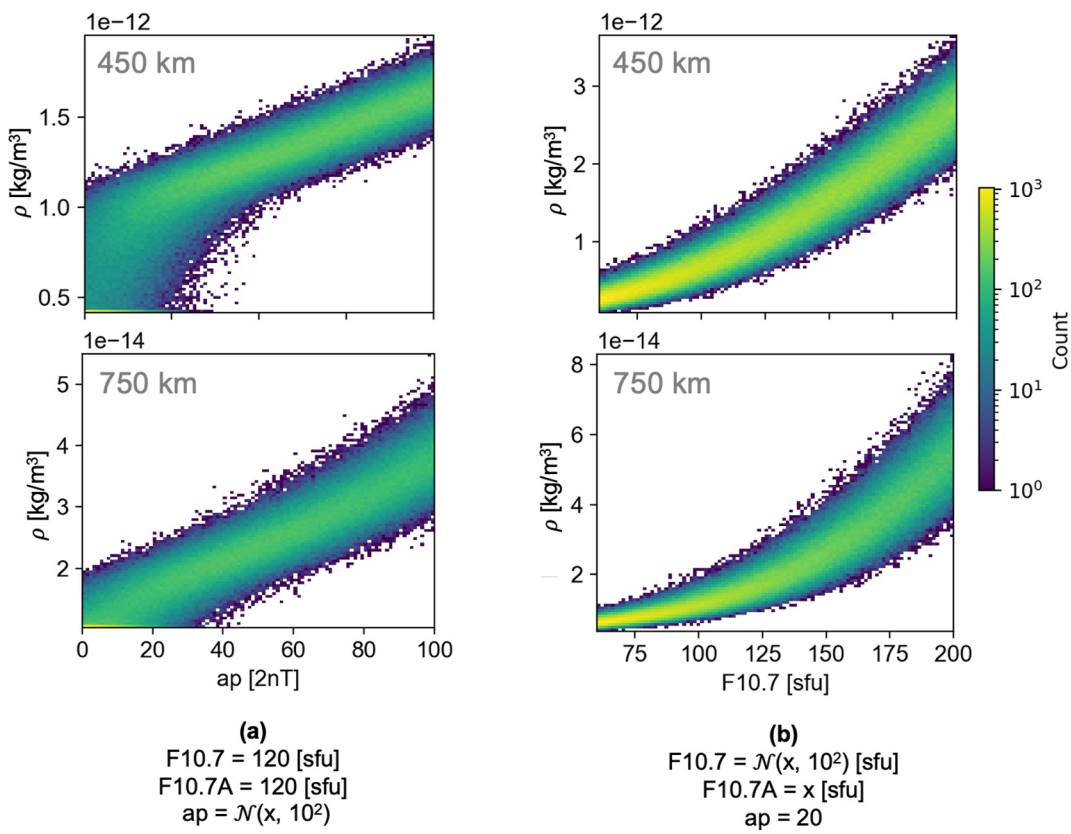

Figure 4. NRLMSISE-00 Densities as computed with Gaussian distributed input uncertainties of (a) $\sigma_{\delta_{ap}} = 10$, (b) $\sigma_{\delta_{F10.7}} = 10$, and means as denoted on the *x*-axis. 450 and 750 km altitudes are shown to demonstrate how heteroscedasticity for density with respect to the drivers changes with altitude.

$ap = \mathcal{N}(x, 10^2)$, while 4(b) shows densities from assuming $F_{10.7} = \mathcal{N}(x, 10^2)$, $F_{10.7A} = x$, and $ap = 20$. For each case, the modeled density is shown for 450 and 750 km altitude. Figure 4a's 450 km case very clearly shows that NRLMSISE-00 modeled density is also heteroscedastic with respect to the mean of the input distribution on *ap*. Above an input mean of 40, the uncertainty in the output appears relatively constant, but below 40, the distribution in density has much greater spread and no longer appears symmetric (especially considering that input *ap* cannot drop below zero, so each negative sampled point is assigned an *ap* of zero). At an altitude of 750 km, uncertainty in *ap* appears much more consistent across input means. Figure 4b repeats the same analysis, but using an uncertain $F_{10.7}$. Interestingly, uncertainty in modeled density appears to be more heteroscedastic with respect to the mean input $F_{10.7}$ with increasing altitude, opposite from what was observed for *ap*. Differences in uncertainty over input mean $F_{10.7}$ are much more apparent at 750 km than they are at 450 km. In Section 5, climatology is used to create an empricical forecast model for the drivers that allows for heteroscedastic, non-Gaussian forecasts.

4. Space Weather and Collision Probability

Over the years, several metrics have been proposed and used in an attempt to quantify the risk of a collision between two resident space objects (RSOs). In the early days, a predicted offset distance was the only parameter considered in the conjunction assessment process (Patera, 2001). But as probabilistic projections of satellite state became available, using deterministic offset distances meant leaving probabilistic information on the table. Today, most operators agree that tracking the probability of collision, computed by considering both the predicted offset distance and the evolved state covariances for the objects of interest (as well as their presumed hard body radii), is a prudent approach to conjunction risk assessment. A satellite operator will generally assign a probability of collision maneuver threshold based on a balance of the risks of a collision and the costs of performing too many maneuvers. NASA generally uses a *Pc* maneuver threshold of 10^{-4} (i.e., a probability of $\frac{1}{10,000}$), while SpaceX generally uses a probability threshold of 10^{-5} (or $\frac{1}{100,000}$). NASA, however, tends to maneuver 24 hr prior to TCA while SpaceX delays maneuvering until 12 hr or less before TCA, which significantly reduces the maneuver burden (Moomey et al., 2023).

When conjunction relative velocities exceed 1 km/s, it becomes reasonable to assume that motion is rectilinear and that the interaction between objects occurs on a plane in the encounter frame of the conjunction. The probability of collision is then a function of the combined hard body radius of the two objects involved in the conjunction, *R*, the position offset vector in the conjunction plane, r_m (with major and minor axis components x_m and y_m), and the 2-dimensional state covariance in the encounter plane with standard deviation components σ_x and σ_y. *Pc* is computed by

$$P_c(R, x_m, y_m, \sigma_x, \sigma_y) = \frac{1}{2\pi\sigma_x\sigma_y}\int_{-R}^{R}\int_{-\sqrt{R^2-x^2}}^{\sqrt{R^2-x^2}} e^{-\frac{1}{2}\left[\left(\frac{x-x_m}{\sigma_x}\right)^2+\left(\frac{y-y_m}{\sigma_y}\right)^2\right]} dy\, dx. \quad (8)$$

Different implementations of solvers for the equation above have been developed over the years that have become increasingly computationally efficient and robust, including (Alfano, 2005; Chan, 1997; Foster & Estes, 1992; Patera, 2001). More information about computing a 2D probability of collision can be found in (Alfano, 2007).

Figure 5 shows that for a conjunction scenario of interest, there are two possible ways to achieve a low *Pc*. The right side of the *Pc* maximum for each curve is called the *dilution region*. It is impossible to achieve a high probability when position uncertainty at TCA is large. Reducing the covariance size (i.e., making better observations and having better predictions) in the diluted region leads to an increase in the *Pc*. To the left of each maximum is what is referred to as the *robust region*. *Pc* is low here when the predicted offset distance is much larger than the uncertainty in object positions. Decreasing covariance size in the robust region leads to a reduction in *Pc*. The ratio of the offset distance to the covariance size is important in determining when the transition into the robust region takes place. Conjunctions that end in a collision will rarely enter the robust region since, at least for well-tracked conjunctions, *Pc* approaches 1 as uncertainty in satellite position at TCA is reduced.

To better understand the impact that poor space weather forecast models can have on *Pc*, a history of real CDMs is useful. In 2019, a set of partial CDMs was publicly released as part of an ESA conjunction assessment challenge (Uriot et al., 2022). An example conjunction from this data set with some of its CDM parameters and relevant

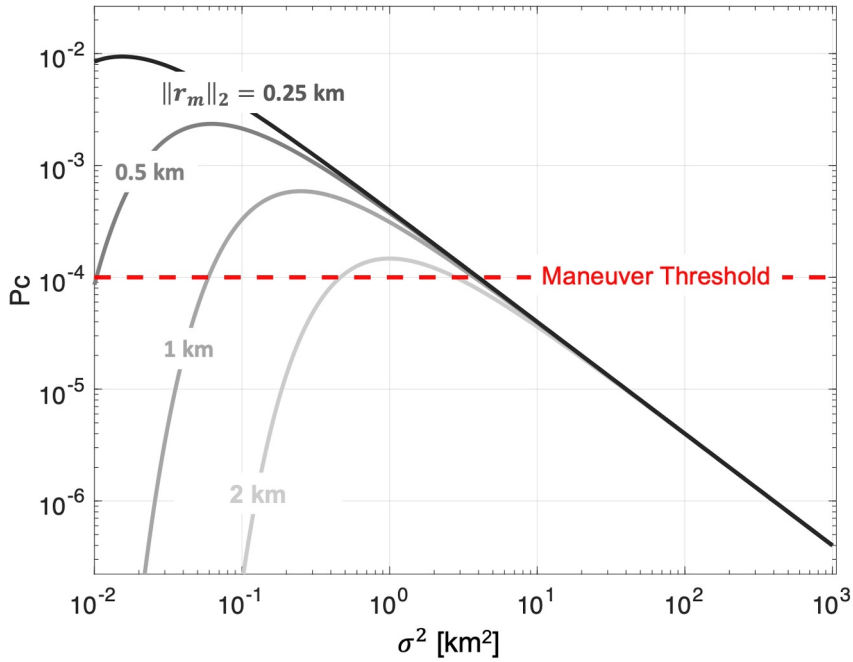

Figure 5. Probability of collision as a function of the position variance and predicted offset distance at TCA. Regions to the right of maximum Pc are considered *diluted*, and maneuver decisions cannot be reliably made here. Increasing the offset distance has the effect of reducing the maximum Pc and pushing this maximum further to the right.

space weather drivers is shown in Figure 6. Unfortunately, the CDMs provided in the data set are anonymized, so the date of this event is unknown. Figure 6a shows $F_{10.7}$ as recorded during this period. These values of $F_{10.7}$ are quite low and relatively stable with no large enhancements or fluctuations. Figure 6b shows the *ap* index values recorded during the conjunction assessment period. The enhancement in *ap* from TCA-4d to TCA-2d might be expected to contribute to neutral density enhancements, which could in turn lead to increased drag on the propagated objects. Figure 6c shows the predicted offset distance from each CDM. Prior to the period of enhanced *ap*, the offset distance is predicted to be large. After seeing increased drag during the period of enhanced geomagnetic activity, however, there is a large drop in the predicted offset distance—making a collision suddenly appear much more likely. If the storm was predicted well, a sudden change in the predicted offset distance wouldn't occur. Figure 6d shows the computed probability of collision for each CDM in the conjunction chain. The *Pc* plot initially shows steady declines in *Pc* as covariance drops with more recent measurements, as expected. Then, when the predicted offset distance drops suddenly following the storm, it is accompanied by a sudden increase in the predicted *Pc*. While *Pc* in this case is below the thresholds for maneuvering, major fluctuations in the predicted *Pc* when close to TCA are problematic since they complicate the maneuver decision-making process. This conjunction series demonstrates the problems that arise when space weather forecasts are not accurate or considered in the conjunction assessment process. Improving space weather forecasts and the way that they are handled in CA is critical for protecting against events like this. Otherwise, the capabilities of the entire CA pipeline will remain diminished during periods of geomagnetic storms and other intervals of enhanced geomagnetic activity.

5. Constructing Empirical Space Weather Driver Forecasts

In order to simulate realistic variability in the drivers (and thus mass density, drag, and satellite state), it is necessary to consider an uncertain forecast model for $F_{10.7}$ and *ap*. In both cases, a procedure built on empirically fitting a distribution to climatology is used. The basis for these forecasts is a persistence assumption. The historical record of the drivers is used to track the distribution of deviations from the persistence forecast. The nominal expected forecast is the expected value of the persistence forecast plus the expected value of the fitted deviation distribution.

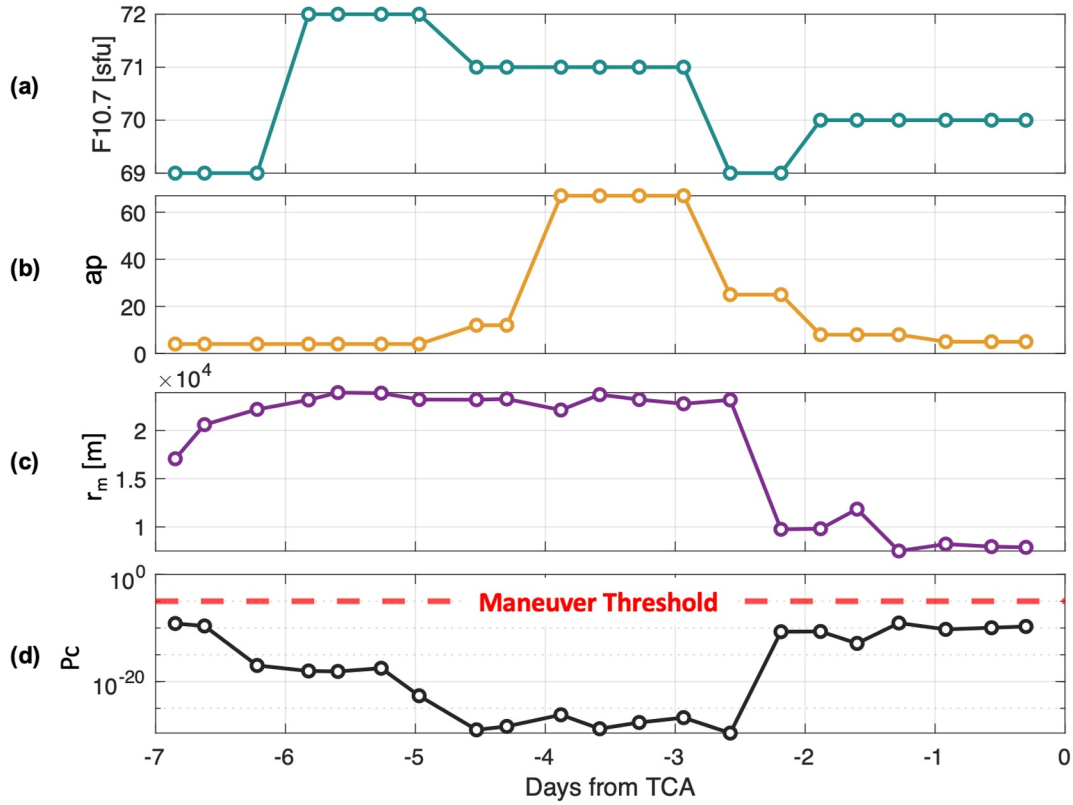

Figure 6. Parameters of interest from a real set of CDMs belonging to a conjunction of interest. (a) Shows $F_{10.7}$ at the time each CDM was generated, (b) shows the three-hour *ap* index, (c) shows the predicted offset distance from each CDM, and (d) shows the resulting *Pc* over time. Large jumps in *Pc* can likely be attributed to poor forecasting of the geomagnetic enhancement apparent in *ap* between TCA - 5days and TCA-2d.

Operational forecasts of *Kp* and *ap* may be slightly better than this simple persistence model, but Figure 2 and Shprits et al. (2019) together suggest that these more complex models will not perform substantially better. Operational forecasts for $F_{10.7}$, however, may be significantly improved by considering recurrence in addition to persistence but a lack of historical forecast record makes it difficult to know what realistic model performance looks like. Closed-source operational forecast models without a published historical record make benchmarking and analysis difficult. This work is left to assume the simple persistance model because of this lack of available data on existing models.

The desired model should accept the current value of the driver of interest along with a desired forecast time horizon. The output is a set of parameters for distribution fit to the observed deviations from the historical record. A distribution of *ap* generally has large gaps (see Figure 3) since discrete values of *Kp* on a scale of 0–9 are mapped to discrete values of *ap*. For this reason, *Kp* was deemed to be better suited for model fitting. A scaled beta distribution is used for *Kp* since it allows for the strict constraints on the upper and lower bound [0, 9], and can incorporate bidirectional skewness when approaching each of those bounds. The location parameter (lowest possible value) on deviation from Kp_0 is $-Kp_0$, and the scale parameter is always 9, since that is the span of *Kp*. The shape parameters a_t and b_t are fitted to the historical deviations at forecast horizon time *t*.

$$F_{Kp}(Kp_0,t) = Kp_0 + \beta(a_t,b_t,-Kp_0,9) \tag{9}$$

It is straightforward to translate between *Kp* and *ap* as needed. Figure 7 shows a sample of the forecast distributions produced when the initial *Kp* is 0, 1, 5, 8, or 9. These values were chosen to highlight the boundedness of the scaled beta distribution within *Kp*'s allowed range. (a) Shows the distributions when the forecast horizon is 3 hr, while (b) shows the distributions from the same initial conditions when the forecast horion is 24 hr. The longer forecast horizon leads to uncertainty distributions with much more spread. These trends (both the skewness

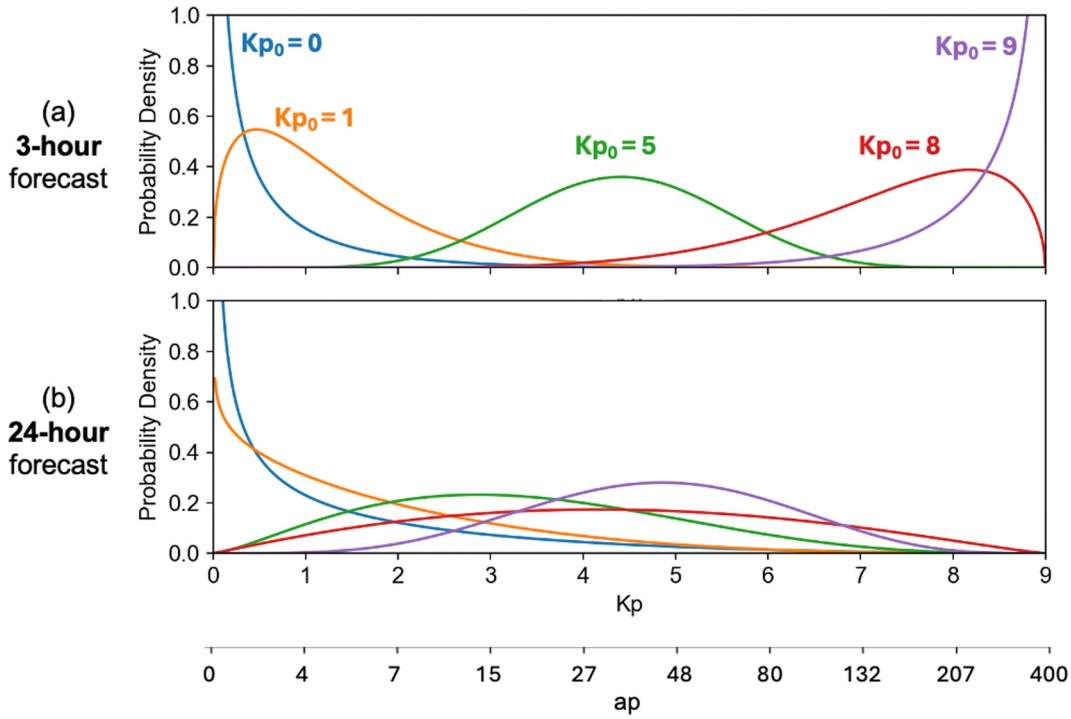

Figure 7. The parameters of a scaled beta distribution is fit to climatology for *Kp*. Provided the current value of *Kp* and the desired forecast time, the simple persistance-based forecast produces an uncertainty distribution. (a) Shows the distributions with a forecast window of 3 hr, while (b) shows the distributions with greater spread after a 24-hr forecast. *Kp* can easily be transformed to *ap* and vice versa. A similar approach is used for modeling $F_{10.7}$, but Gaussian distributions are used.

near the bounds and the spreading with increasing forecast time) are plainly apparent in Figures 3 and 2, respectively. Eventually, with enough time horizon, the forecasts should all start to converge on the climatological average distribution for *Kp*.

A similar process was carried out for modeling $F_{10.7}$ (not shown in the figure), but a Gaussian distribution is used instead of a scaled beta distribution. Since $F_{10.7}$ is not discrete like *Kp*, a binning approach was required to determine forecast uncertainty parameters from the climatology. A history of forecast errors was first computed for each of 50 bins from 60 sfu to 450 sfu (each bin is approximately 8 sfu wide). The last known value of $F_{10.7}$ determines the reference bin, while the lookahead window is considered when sampling the historical deviations from the start values within the bin. Since $F_{10.7}$ is only released once per day, only forecast periods in daily increments are possible. Thus, given a start value and a desired lookahead time, the persistence forecast with uncertainty bounds for $F_{10.7}$ may be computed by

$$F(F_{10.7},t) = F_{10.7_0} + \mathcal{N}(\mu_t,\sigma_t^2). \tag{10}$$

Similarly to *Kp*, the $F_{10.7}$ forecast uncertainty spreads with horizon time in general. These forecast models are used to generate sampled driver forecasts within the prescribed uncertainty distributions in the simulation results section below. For detailed analysis on how satellite state perturbations evolve from uncertain space weather driver forecasts, see the Appendix A.

6. Simulation Results

The newly developed heteroscedastic driver forecast models will be applied to real historical driver data from the seven-day period from 27 October 2003 00 UTC to 3 November 2003 00z. This period was selected because it includes the Halloween storm of 2003. Beginning with known start drivers, 7 days' worth of forecast distributions were computed for $F_{10.7}$ and *Kp*. Figures 8a and 8b show the true values for the drivers along with 100 potential

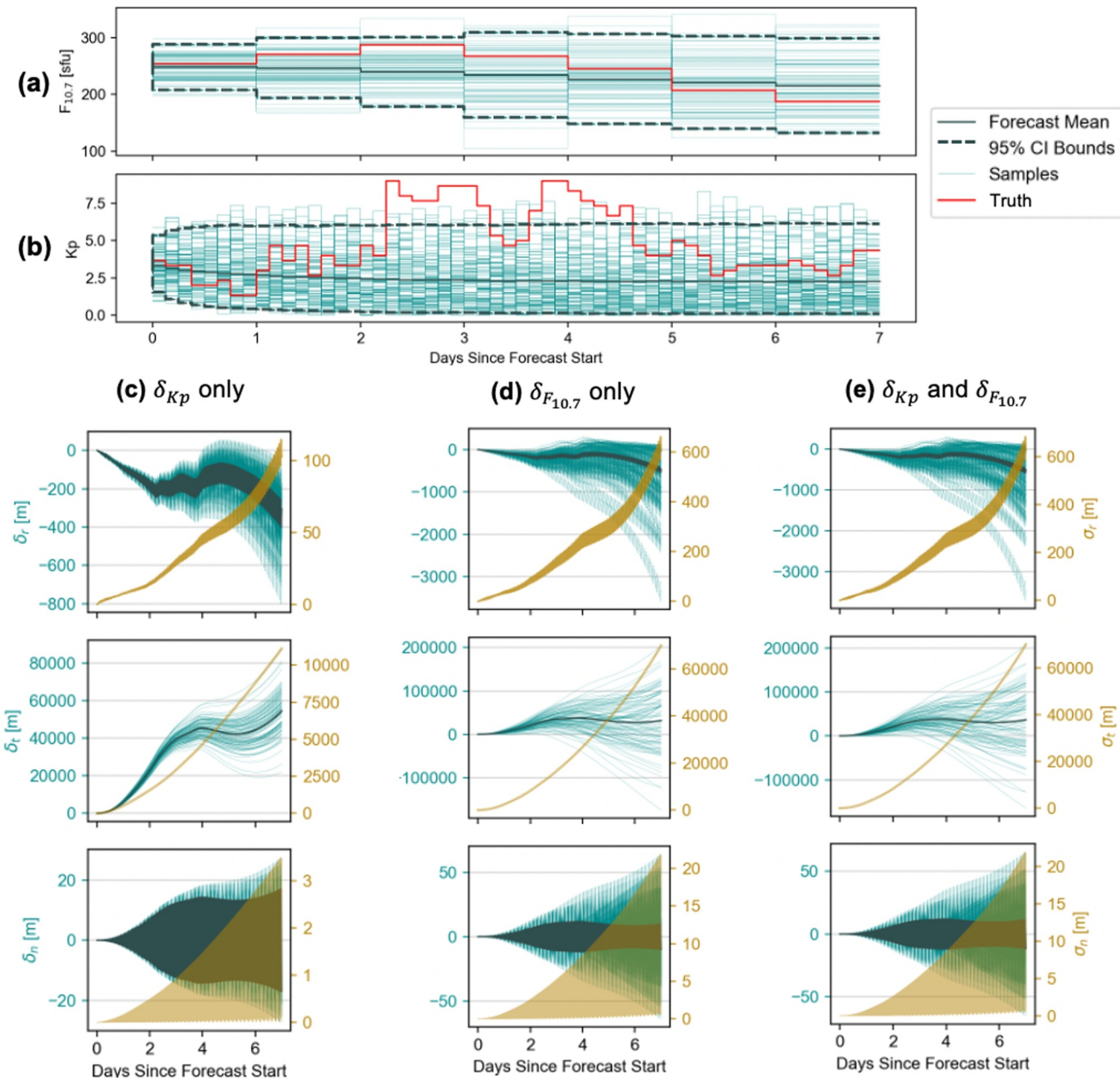

Figure 8. 100 samples deviating from a reference truth state from October 27 to 3 November 2003 according to climatological driver uncertainty. (a) Shows sample deviations in the $F_{10.7}$ proxy, (b) shows sample deviations in *Kp*. After propagating a spacecraft through modeled density from these sampled drivers, (c) shows RTN position errors considering only δ_{Kp}, (d) shows RTN position errors considering only $\delta_{F_{10.7}}$, and (e) shows RTN position errors showing the combined effect of both $\delta_{F_{10.7}}$ and δ_{Kp}.

driver trajectories sampled from the uncertainty distribution at each timestep. Each set of driver trajectories corresponds to a different atmospheric profile for a satellite to be propagated through. Three example cases are explored to trace the impact of uncertainty in each driver on satellite state and collision probability.

- **Case (1)** considers $F_{10.7}$ known and *Kp* uncertain
- **Case (2)** considers $F_{10.7}$ uncertain and *Kp* known
- **Case (3)** considers both $F_{10.7}$ uncertain and *Kp* uncertain

If $F_{10.7}$ or *Kp* are presumed known, the true value over the time period of interest is used in propagation. Figure 8c, d, and e show propagated position deviations in the radial, along-track, and normal (RTN) component directions

for an object with $B = 0.02$ m^2/kg, initial altitude of 550 km, eccentricity of zero, and inclination of 80°. The evolved satellite positions were computed using a propagator that considered Keplerian dynamics with a corrector term for Earth's J2 oblateness and a variable atmospheric density term for each timestep. The satellite was propagated first assuming no drag to query rough orbital positions, then neutral mass density was computed at each position using NRLMSISE-00 for each timestep according to the sampled space weather driver forecast.

The first column, 8(c), shows the deviations in positions from a forecast where only *Kp* is uncertain. The magnitude of the position deviation is much larger in the along-track component than in the radial component, which is also much larger than the deviation in the normal component. This agrees with intuition from Equations A4 and A5 in the Appendix A, which suggest that along-track error should grow proportionally to the integral of the normalized forecast density error and that the radial component would grow proportionally to the double-integral of the forecast density error. The normal component deviation is small because it is driven by a slow plane-change, and indeed it oscillates between bounds as was predicted in Equation A14. The mean position error in the radial and along-track directions diverges quickly from zero before the error growth rate is slowed during the period of geomagnetic activity enhancement during the storm (between days 2–5 from forecast start). In this case, the storm acted to balance an existing bias in the sample forecasts that existed prior to the storm.

Figure 8d shows the deviations along the orbital path when there is only uncertainty in the forecasted $F_{10.7}$. While the relative magnitudes of the deviations between the components remain similar to what was found in (c), the actual magnitudes are much larger since thermospheric mass density is very sensitive to changes in EUV flux. Figure 8e shows the combined effect of forecast uncertainty in both *Kp* and $F_{10.7}$. Since the magnitude of deviations in the $F_{10.7}$-deviated case significantly outweigh those from the *Kp*-deviated case, the distributions look similar between (*e*) and (d). These propagations suggest that uncertainty in $F_{10.7}$ plays a more significant role in determining satellite position uncertainty than uncertainty in forecasted *Kp*. We would expect that variability in *Kp* would have a large impact on satellite drag for this scenario in particular because it is highly inclined and passes through the auroral regions, yet uncertainty in $F_{10.7}$ still appears dominant.

Now, this propagation will be applied to an example conjunction scenario to investigate how space weather forecasting uncertainty impacts *Pc* and maneuver decisions. To simulate an informative set of scenarios, a starting satellite state is initialized for a circular orbit at 650 and 850 km initial altitude, each with an inclination of 80°. The same time period of interest (27 October 2003 00 UTC to 3 November 2003 00z) is considered.

Starting at the initial time, 100 sample satellites with perfect initial state knowledge are propagated forward. The atmospheric density profile that each object travels through is computed by sampling deviations on $F_{10.7}$ and *Kp* as shown in Figures 8a and 8b. A reference object is also propagated using the true space weather drivers during this period. At 3-hr intervals, a new set of propagated objects is initialized at the location of the reference point for each step. This process simulates taking new measurements every 3 hours that constrain state uncertainty at that time to zero. The expected state and covariance at TCA for each iteration will differ because the first iteration will have been propagated for 7 days, the second for 6 days 21 hr, and so on. The probability of collision at TCA is computed using Equation 8 based on these expected states and covariances, which allows us to compare the computed probability of collision as a function of time until TCA under a variety of circumstances.

To emphasize a critical scenario, a true collision is simulated where the primary object (being tracked) and secondary object have a true final centroid position offset, $r_m = [0.1, 0.1, 0.1]$ m and each object involved in the conjunction has a hard body radius of 30 m. Such a small centroid offset for a combined hard body radius of 60 m means that this collision will surely occur.

The velocity of the secondary object relative to the primary object can play an impactful role in the probability of collision, so this scenario selects a random uniform sample of 1,000 relative velocity magnitudes on the interval [5, 15] km/s. The relative velocity direction is computed by a uniform random sample of 1,000 unit vector directions. This stochastic approach to modeling potential conjunction geometries is critical for getting a fuller picture of potential maneuver decisions. To keep the example simple, the state covariance matrix for the secondary object at TCA in all cases is the same as the covariance of the primary, just oriented in the RTN frame with respect to the secondary object rather than the primary. Still, the assumption that the covariances are not correlated when computing the probability of collision is retained for a more realistic *Pc* evaluation.

Figure 9 shows the probability that the computed *Pc* exceeds a maneuver threshold of 1×10^{-4} as a function of time until TCA for each of the example cases. The period from −7 to −4 days from TCA is excluded from the

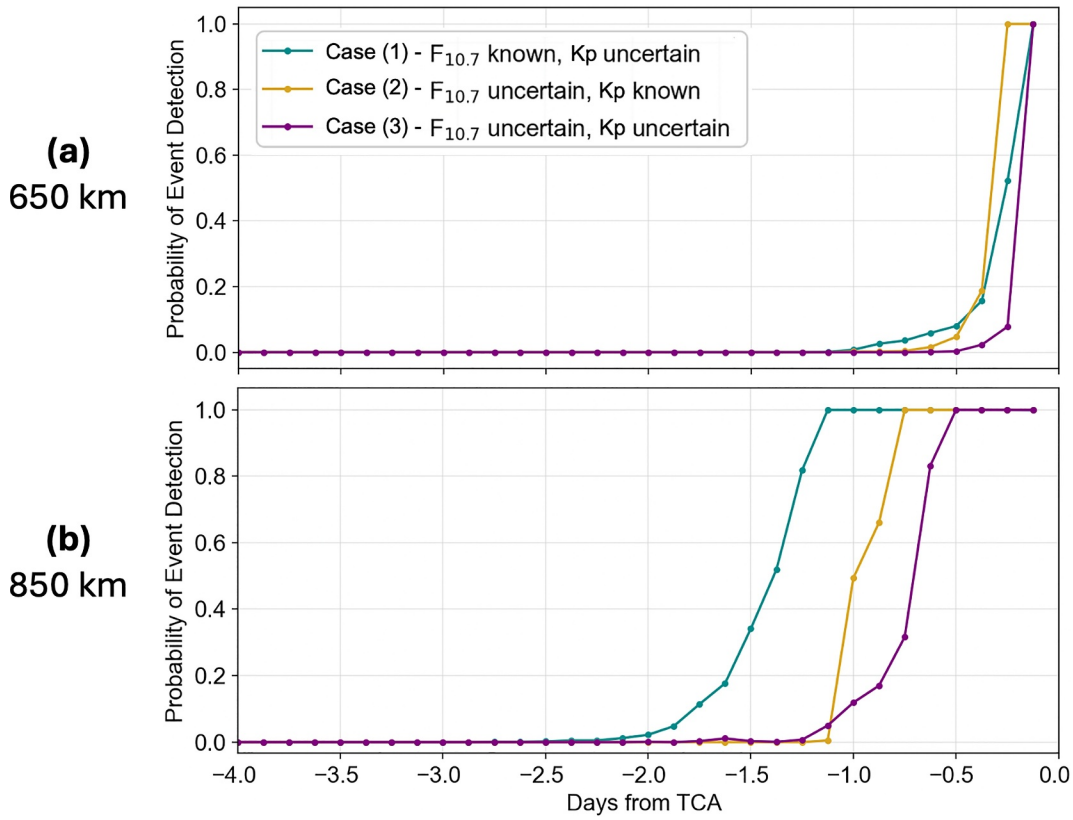

Figure 9. Probability of maneuvering for a conjunction event that ends in a collision as a function of time from TCA. Maneuver decisions are based on a *Pc* threshold of 10^{-4} and each case is demonstrated at (a) 650 km, (b) 850 km to show altitude dependence. This comparison is done is at solar maximum (TCA is 3 November 2003). Altitude dependence will change according to the solar cycle.

plots because there was zero probability of detection during this period. Figure 9a shows maneuver decision probabilities by case at an altitude of 650 km, while (b) shows 850 km. If a maneuver decision needed to be made *n* days prior to TCA, the figure shows what decision might be made for each of the three cases at the two query altitudes. The plot demonstrates that, considering climatological uncertainty in the driver forecasts, it is difficult to make correct maneuver decisions early at 650 km under any circumstance during the study period. Case (3) shows that a correct maneuver decision cannot be reliably made until only 3 hours prior to TCA. Even removing uncertainty in $F_{10.7}$ altogether in case (1) provides very little additional notice. Removing the uncertainty in *Kp* in case (2) makes a similar impact on maneuver decision time at 650 km. In all cases, the uncertainty in the drivers makes it very difficult for Pc to be large enough to justify a maneuver until just before TCA. It is important to remember that measurement uncertainty is neglected for this scenario, so if both indices were certain an operator would have perfect knowledge of the conjunction at all times and would know to maneuver as soon as the conjunction was identified.

At 850 km altitude, there is a clearer difference between the cases since drag is not as impactful at this altitude in perturbing the satellite state. Case (1) offers nearly 24 hr of additional maneuver notice over case (3). Case (2) offers slight improvement over the baseline case (3). Even case (3) can make a good maneuver decision 12 hr prior to TCA. Again, we see that there is potentially more value in reducing forecast uncertainty for $F_{10.7}$ as opposed to *Kp*, even though $F_{10.7}$ is less susceptible to rapid and unpredictable enhancements. The sensitivity of neutral density to variability in $F_{10.7}$ should not be underestimated. At higher altitudes it takes a long time for satellite position errors to accumulate from changes in density, so maneuver decisions earlier than the standard 12–24 hr may be generally feasible across a wide variety of environmental conditions. It stands to reason that at even higher altitudes where the baseline density of the atmosphere is very low, space weather forecasts make little difference in conjunction assessment since they would be well characterized from the very beginning.

In general, the altitude region where space weather forecasts are useful for conjunction assessment will vary with the solar cycle. This effort has shown that there is a region below which forecast uncertainty paralyzes decision-makers by diluting confidence in satellite state. This is clearly apparent at 650 km in Figure 9. It is also possible to show that there is an upper bound in altitude where the baseline drag is so low that space weather forecasts do not make an actionable difference. The useful region characterized by these upper and lower bounds will shift upwards during solar maximum and downward during solar minimum.

7. Conclusion

This work has highlighted some of the challenges in interpreting and using forecasts of the space weather drivers for satellite conjunction assessment. First, it was shown that the popular deterministic driver forecast models generally perform more poorly in and around solar maximum, just when neutral density is large enough in LEO for drag uncertainty to become very important for satellite conjunction assessment. Then, historical error distributions on persistence models were used to show that forecasts of the drivers are heteroscedastic, where the uncertainty in the predicted value for a driver depends on the start value and the time horizon of interest. The geomagnetic index *Kp* (along with its derived *ap* and *Ap*) represents a unique challenge in that uncertainty distributions for this index regularly exhibit significant skewness when approaching the bounds on possible values. Even if driver uncertainty distributions were Gaussian, NRLMSISE-00 and other atmospheric models produce a nonlinear mapping from driver uncertainty to neutral density uncertainty which can further complicate conjunction assessment.

An empirical heteroscedastic forecast model was developed for *Kp* and $F_{10.7}$ which allowed us to simulate satellite motion with uncertain drag. It was found that, at least for the time period of the study, uncertainty in $F_{10.7}$ is the dominant contributor to satellite state uncertainty, even though forecasts of *Kp* were much poorer. Large geomagnetic activity enhancements are rare, but can cause large increases in density on very short timescales. Handling forecasts of *Kp* with skewed distributions allows us to appropriately consider the probability of these rare events, though it might take several solar cycles for them to occur. A conjunction simulation showed that a forecast model with known $F_{10.7}$ had the potential to provide more than 24 hr' advance maneuver notice over the models that used an uncertain $F_{10.7}$, though the impact of driver uncertainty on satellite drag varies with altitude, inclination, and the solar cycle. Future work will investigate the actual error performance of real forecasts compared to the simple empirical and persistence-based forecasts used in this work. The procedure used in this effort may also be extended to investigate uncertainty in the forecasts for other drivers used in higher-fidelity atmospheric models.

It is difficult to investigate and understand the consequences of driver forecast uncertainty when space weather agencies provide a deterministic expected forecast without uncertainty. The satellite operator community could substantially benefit from being provided forecast uncertainties rooted in the physics behind the drivers. As it stands today, operators are left to rely on their own empirical assessment of forecast error performance to estimate uncertainty (as was done in this work). Some operators may even assume that the provided forecasts are perfect, an assumption which leads to poor covariance realism, and potentially an unanticipated collision. Accurately representing and communicating the uncertainty in the forecasted drivers can be complicated for non-Gaussian, heteroscedastic forecasts, but that uncertainty distribution information is critical for improving the satellite conjunction assessment process and avoiding dangerous collisions in orbit.

Appendix A: Satellite State Perturbations in Dynamic Drag Environments

Various approaches have been implemented in practice to propagate spacecraft state uncertainty considering the influences of space weather effects throughout the propagation. Most operational methods feed the forecasted space weather drivers through an empirical model for neutral density. This nominal density profile is then used to propagate the state of the spacecraft. Clearly, there is some uncertainty in the model and in the forecast that needs to be accounted for in this propagation in order to accurately represent the satellite state covariance at the time of closest approach. In practice, this uncertainty quantification is often performed by again employing an empirical model that considers historical error in neutral mass density predictions as a function of the space weather conditions (i.e., during quiet, moderate, or storm-time environments). Uncertainty in the density is then captured in the propagation by adding a "consider parameter," a scaling factor that artificially inflates uncertainty in the B^* term (M. Hejduk, 2019; Poore et al., 2016; Barker et al., 2000). Assigning additional (typically Gaussian)

uncertainty to B^* conflates sources of error from ballistic coefficient terms (satellite attitude and mass) with atmospheric density, which makes analysis of uncertainty contributions difficult. Ideally, uncertainty in atmospheric density, and thus propagated satellite state, should be derived analytically from the root causes: uncertainty in the forecasted space weather drivers and uncertainty in the atmospheric model.

Drag influences the mean motion of a satellite's orbit by

$$\dot{n} = \frac{3}{2} n^{1/3} \mu^{-2/3} \rho B v^3 F \tag{A1}$$

where $n = \sqrt{\mu / a^3}$ is the mean motion, a is the semi-major axis, μ is the gravitational parameter, ρ is the neutral mass density, v is the orbital speed, and F is a factor based on the thermospheric winds:

$$F = \frac{\|\mathbf{v} - \mathbf{v}_A\|^2}{v^2} \mathbf{e}_{\mathbf{v}} \cdot \mathbf{e}_{\mathbf{v}-\mathbf{v}_A} \tag{A2}$$

where $\mathbf{v}$ is satellite velocity, $\mathbf{v}_A$ is the velocity of the atmosphere, and $\mathbf{e}_{\mathbf{v}}$ and $\mathbf{e}_{\mathbf{v}-\mathbf{v}_A}$ are unit vectors in the subscripted vector directions. The mean anomaly may be computed from mean motion by

$$\frac{dM}{dt} = n. \tag{A3}$$

J. T. Emmert et al. (2017) derived the following analytical expressions for the deviation in the n and M as a function of the relative neutral density error, ϵ_ρ integrated along the orbital path:

$$\delta_n(t) \approx \delta_{n_0}\left(1 + \frac{1}{3}\frac{\Delta\hat{n}}{\Delta\hat{n}_0}\right) + \frac{\Delta\hat{n}}{\Delta t}\int_{t_0}^{t} \epsilon_\rho\left(t'\right) dt' \tag{A4}$$

$$\delta_M(t) \approx \delta_{M_0} + \delta_{n_0}\Delta t\left(1 + \frac{1}{6}\frac{\Delta\hat{n}}{\hat{n}_0}\right) + \frac{\Delta\hat{n}}{\Delta t}\int_{t_0}^{t}\int_{t_0}^{t'} \epsilon_\rho(t'')\, dt''\, dt' \tag{A5}$$

where δ_{n_0} and δ_{M_0} are the initial measurement errors for the mean motion and mean anomaly, respectively, and $\Delta\hat{n}$ and $\hat{n}_0$ are the estimated change in mean motion and initial mean motion, respectively. The relative error is defined as

$$\epsilon_\rho(t) = \frac{\hat{\rho}(t) - \rho(t)}{\rho(t)}. \tag{A6}$$

We define $n_{ref}\,(t)$ and $M_{ref}\,(t)$ as the reference values in n and M using the true density. Thus $\epsilon_\rho = 0$ for the reference case. $n_{ref}\,(t)$ and $M_{ref}\,(t)$ may be computed by numerical propagation through the real atmospheric density profile along the orbital path. When starting from perfectly known n and M, Equations A4 and A5 show that error over time in n is proportional to the first integral of the normalized density error, while error in M is proportional to the second integral of the normalized density error. For Pc computation, however, we are interested in deviations in the spacecraft-fixed frame defined by the radial, along-track, and normal (RTN) components (δ_r, δ_t, δ_n). The unit vectors for this coordinate frame may be computed from an Earth-centered inertial position $\mathbf{r}$ and velocity $\mathbf{v}$ where

$$\mathbf{e}_r = \frac{\mathbf{r}}{\|\mathbf{r}\|}, \mathbf{e}_n = \frac{\mathbf{r} \times \mathbf{v}}{\|\mathbf{r} \times \mathbf{v}\|}, \mathbf{e}_t = \mathbf{e}_n \times \mathbf{e}_r \tag{A7}$$

An approximate conversion from δ_n and δ_M to δ_r and δ_t, respectively, is relatively straightforward from Keplerian dynamics. For position errors that are small relative to the curvature of the orbit path, the radial component of the deviation relates to a change in the semi-major axis of the ellipse, the along-track component relates to the deviation in true anomaly. The normal component relates to small plane changes that occur when the right ascension

of the ascending node (RAAN, Ω) drifts at slightly different rates as the semi-major axis changes throughout the propagation. This nodal drift may be approximated using J_2 perturbations.

Using Earth's gravitational parameter $\mu = 398{,}600\ \mathrm{km}^3/\mathrm{s}^2$, the semi-major axis of the orbit may be computed from $n(t) = n_0 + \delta_n(t)$ directly

$$a(t) = \left(\frac{\mu}{(n(t))^2}\right)^{1/3}. \tag{A8}$$

The eccentric anomally can be solved for numerically from $M(t) = M_0 + \delta_M(t)$ by the following relation:

$$M(t) = E(t) - e\sin(E(t)) \tag{A9}$$

where e is the eccentricity of the orbit. Once $a(t)$ and $E(t)$ are known, the radial distance along the deviated orbit path is simply

$$r(t) = a(t)(1 - e\cos(E(t))). \tag{A10}$$

To determine the deviation in position along the radial component from the reference state, simply compute $\delta_r = r_{dev}(t) - r_{ref}(t)$, where r_{ref} is the radius computed using n_{ref} and M_{ref} with true atmospheric density, while r_{dev} is computed using the deviated density profile.

The along-track satellite position offset, δ_t, is more simply related to the deviation in mean anomaly by

$$\delta_t(t) \approx \delta_M(t)\frac{\hat{v}(t)}{\hat{n}(t)}, \tag{A11}$$

where $\hat{v}$ and $\hat{n}$ are the estimated velocity and mean motion. Now that the radial and along-track components of the deviation are known, the normal component may be approximated by considering the precession rate of the right ascension of the ascending node, $\dot{\Omega}$, due to J_2 perturbations

$$\dot{\Omega} = -\frac{3}{2}J_2\left(\frac{R_E}{a(1-e^2)}\right)^2\sqrt{\frac{\mu}{a^3}}\cos i \tag{A12}$$

where J_2 is Earth's J_2 parameter (1.0826×10^{-3}), R_E is the average radius of the Earth (6,378.15 km), and i is the inclination of the orbit (Vallado, 2001). The inclination is assumed constant. Since the forecasted satellite propagations required for conjunction assessment typically have less than a 7-day time horizon, it is reasonable to approximate the eccentricity as constant as well. Now, a is the only time-varying parameter that $\dot{\Omega}$ depends on. As small changes in a occur during the orbital propagation, differences in the nodal drift rate will accumulate to cause minor shifts in the orbital plane. This out-of-plane perturbation leads to position deviation in the cross-track component, δ_n. δ_c may be approximated by first considering the angle δ_Ω between the orbit planes

$$\delta_\Omega(t) = \int_0^t \left(\dot{\Omega}_{dev} - \dot{\Omega}_{ref}\right) t'\,dt'. \tag{A13}$$

Then, the position deviation in the cross-track component is approximately bounded by

$$\|\delta_n(t)\| < 2\bar{a}_{ref}(1+e)\sin(\delta_\Omega(t)). \tag{A14}$$

This is a bound because deviation along the normal component will oscillate as a function of time since the deviated and reference orbital planes intersect to cause two crossings along the orbital path.

Data Availability Statement

Historical TLEs for tracked objects are publicly available through space-track.org. Partial historical CDMs were accessed and are available from https://kelvins.esa.int/collision-avoidance-challenge/data/. A history of the recorded space weather drivers is available at https://kp.gfz-potsdam.de/en/data. NOAA's Space Weather Prediction Center's forecast verification page is accessible at https://www.swpc.noaa.gov/content/forecast-verification.

Acknowledgments
This work was supported by the National Science Foundation Graduate Research Fellowship under Grant 1745302 and the National Science Foundation under award NSF-PHY-2028125. Mervyn Freeman, Gareth Chisham, and Andrew Kavanagh were supported by core funding from the UK Natural Environment Research Council to the British Antarctic. The authors gratefully acknowledge the sponsors for their support.

References

Alfano, S. (2005). A numerical implementation of spherical object collision probability. *Journal of the Astronautical Sciences*, *53*(1), 103–109. https://doi.org/10.1007/bf03546397

Alfano, S. (2007). Review of conjunction probability methods for short-term encounters (aas 07-148). *Advances in the Astronautical Sciences*, *127*(1), 719.

Aristoff, J. M., Cox, C. M., Nasa, J. H. F., Grumman, R. W. G. N., Horwood, J. T., Jah, M. K., et al. (2016). Covariance and uncertainty realism in space surveillance and tracking.

Barker, W. N., Casali, S. J., & Walker, C. A. (2000). Improved space surveillance network observation error modeling and techniques for force model error mitigation. *Astrodynamics*, *1999*, 1881–1901.

Bartels, J. (1949). The standardized index, ks, and the planetary index, kp. *IATME bull*, *97*(0001).

Bowman, B. (2002). True satellite ballistic coefficient determination for hasdm. In *Aiaa/aas astrodynamics specialist conference and exhibit* (p. 4887).

Bowman, B., Tobiska, W. K., Marcos, F., Huang, C., Lin, C., & Burke, W. (2008). A new empirical thermospheric density model jb2008 using new solar and geomagnetic indices. In *Aiaa/aas astrodynamics specialist conference and exhibit* (p. 6438).

Bruinsma, S. (2015). The dtm-2013 thermosphere model. *Journal of Space Weather and Space Climate*, *5*, A1. https://doi.org/10.1051/swsc/2015001

Bussy-Virat, C. D., Ridley, A. J., & Getchius, J. W. (2018). Effects of uncertainties in the atmospheric density on the probability of collision between space objects. *Space Weather*, *16*, 519–537. https://doi.org/10.1029/2017SW001705

Chan, K. (1997). Collision probability analysis for earth orbiting satellites. *Space cooperation into the 21 st century*, 1033–1048.

Covington, A. (1948). Solar noise observations on 10.7 centimeters. *Proceedings of the IRE*, *36*(4), 454–457. https://doi.org/10.1109/JRPROC.1948.234598

Davis, E., Dunn, C., Stanton, R., & Thomas, J. (2000). The grace mission: Meeting the technical challenges. *Technical Reports Series*.

Dickey, M. R., & Culp, R. D. (1989). Determining characteristic mass for low-earth-orbiting debris objects. *Journal of Spacecraft and Rockets*, *26*(6), 460–464. https://doi.org/10.2514/3.26092

Doornbos, E., Förster, M., Fritsche, B., van Helleputte, T., van den Ijssel, J., Koppenwallner, G., et al. (2009). Air density models derived from multi-satellite drag observations. In *Proceedings of esas second swarm international science meeting. potsdam* (Vol. 24).

Emmert, J., Dhadly, M., & Segerman, A. (2021a). A globally averaged thermospheric density data set derived from two-line orbital element sets and special perturbations state vectors. *Journal of Geophysical Research: Space Physics*, *126*(8), e2021JA029455. https://doi.org/10.1029/2021ja029455

Emmert, J. T., Drob, D. P., Picone, J. M., Siskind, D. E., Jones, M., Jr., Mlynczak, M., et al. (2021b). Nrlmsis 2.0: A whole-atmosphere empirical model of temperature and neutral species densities. *Earth and Space Science*, *8*(3), e2020EA001321. https://doi.org/10.1029/2020ea001321

Emmert, J. T., Warren, H., Segerman, A., Byers, J., & Picone, J. (2017). Propagation of atmospheric density errors to satellite orbits. *Advances in Space Research*, *59*(1), 147–165. https://doi.org/10.1016/j.asr.2016.07.036

Foster, J. L., & Estes, H. S. (1992). A parametric analysis of orbital debris collision probability and maneuver rate for space vehicles. *NASA, National Aeronautics and Space Administration, Lyndon B. Johnson Space Cene*.

George, E., & Harvey, S. (2011). A comparison of satellite conjunction analysis screening tools. Report), air force research lab Kirtland AFB NM space vehicle directorate.

Gondelach, D. J., Armellin, R., & Lidtke, A. A. (2017). Ballistic coefficient estimation for reentry prediction of rocket bodies in eccentric orbits based on tle data. *Mathematical Problems in Engineering*, *2017*, 1–13. https://doi.org/10.1155/2017/7309637

Gondelach, D. J., Linares, R., & Siew, P. M. (2022). Atmospheric density uncertainty quantification for satellite conjunction assessment. *Journal of Guidance, Control, and Dynamics*, *45*(9), 1760–1768. https://doi.org/10.2514/1.g006481

Hejduk, M. (2019). Three ca-related covariance issues and their solutions. In *Cnes international conjunction assessment workshop*.

Hejduk, M., & Pachura, D. (2017). Conjunction assessment screening volume sizing and event filtering in light of natural conjunction event development behaviors. In *Aas/aiaa astrodynamics specialists conference*.

Hejduk, M. D., & Snow, D. E. (2018). The effect of neutral density estimation errors on satellite conjunction serious event rates. *Space Weather*, *16*, 849–869. https://doi.org/10.1029/2017SW001720

Henney, C., Hock, R., Schooley, A., Toussaint, W., White, S., & Arge, C. (2015). Forecasting solar extreme and far ultraviolet irradiance. *Space Weather*, *13*(3), 141–153. https://doi.org/10.1002/2014sw001118

Henney, C., Toussaint, W., White, S., & Arge, C. (2012). Forecasting f10. 7 with solar magnetic flux transport modeling. *Space Weather*, *10*(2). https://doi.org/10.1029/2011sw000748

Hoots, F. R. (1980). Spacetrack report no. 3, models for propagation of norad element sets. http://www.itc.nl/-bakker/orbit.html

Krage, F. J. (2023). Nasa spacecraft conjunction assessment and collision avoidance best practices handbook (Tech. Rep.).

Lean, J., Picone, J., & Emmert, J. (2009). Quantitative forecasting of near-term solar activity and upper atmospheric density. *Journal of Geophysical Research*, *114*(A7). https://doi.org/10.1029/2009ja014285

Licata, R. J., Tobiska, W. K., & Mehta, P. M. (2020). Benchmarking forecasting models for space weather drivers. *Space Weather*, *18*(10), e2020SW002496. https://doi.org/10.1029/2020sw002496

Linares, R., Crassidis, J. L., & Jah, M. K. (2014). Particle filtering light curve based attitude estimation for non-resolved space objects. In *Aas/aiaa space flight mechanics meeting* (pp. 14–210).

Moomey, L. C. D., Falcon, R., & Khan, A. (2023). Trending and analysis of payload vs. all low earth conjunction data messages below 1000 km, from 2016 through 2021. *Journal of Space Safety Engineering*, *10*(2), 217–230. https://doi.org/10.1016/j.jsse.2023.03.006

NASA. (2023). Cost and benefit analysis of orbital debris remediation. Retrieved from https://www.nasa.gov/sites/default/files/atoms/files/otps_-_cost_and_benefit_analysis_of_orbital_debris_remediation_-_final.pdf. Accessed 7 April 2023.
NOAA Space Weather Prediction Center. (n.d.). Forecast verification. Retrieved from https://www.swpc.noaa.gov/content/forecast-verification. Accessed 3 April 2024.
Paouris, E., Abunina, M., Belov, A., & Mavromichalaki, H. (2021). Statistical analysis on the current capability to predict the ap geomagnetic index. *New Astronomy*, *86*, 101570. https://doi.org/10.1016/j.newast.2021.101570
Patera, R. P. (2001). General method for calculating satellite collision probability. *Journal of Guidance, Control, and Dynamics*, *24*(4), 716–722. https://doi.org/10.2514/2.4771
Picone, J., Hedin, A., Drob, D. P., & Aikin, A. (2002). Nrlmsise-00 empirical model of the atmosphere: Statistical comparisons and scientific issues. *Journal of Geophysical Research*, *107*(A12), SIA–15. https://doi.org/10.1029/2002ja009430
Poore, A. B., Aristoff, J. M., Horwood, J. T., Armellin, R., Cerven, W. T., & Cheng, Y. (2016). Covariance and uncertainty realism in space surveillance and tracking. *Report of the Air Force Space Command Astrodynamics Innovation Committee*, *27*.
Reigber, C., Schwintzer, P., & Lühr, H. (1999). The champ geopotential mission. *Boll. Geof. Teor. Appl*, *40*, 285–289.
Saunders, A., Swinerd, G. G., & Lewis, H. G. (2012). Deriving accurate satellite ballistic coefficients from two-line element data. *Journal of Spacecraft and Rockets*, *49*(1), 175–184. https://doi.org/10.2514/1.56603
Schildknecht, T., Silha, J., Pittet, J.-N., & Rachman, A. (2017). Attitude states of space debris determined from optical light curve observations.
Shprits, Y. Y., Vasile, R., & Zhelavskaya, I. S. (2019). Nowcasting and predicting the kp index using historical values and real-time observations. *Space Weather*, *17*(8), 1219–1229. https://doi.org/10.1029/2018SW002141
Šilha, J. (2020). Space debris: Optical measurements. *Reviews in Frontiers of Modern Astrophysics: From Space Debris to Cosmology*, 1–21. https://doi.org/10.1007/978-3-030-38509-5_1
Šilha, J., Pittet, J.-N., Hamara, M., & Schildknecht, T. (2018). Apparent rotation properties of space debris extracted from photometric measurements. *Advances in Space Research*, *61*(3), 844–861. https://doi.org/10.1016/j.asr.2017.10.048
Storz, M. F., Bowman, B. R., Branson, M. J. I., Casali, S. J., & Tobiska, W. K. (2005). High accuracy satellite drag model (hasdm). *Advances in Space Research*, *36*(12), 2497–2505. https://doi.org/10.1016/j.asr.2004.02.020
Tapping, K. (2013). The 10.7 cm solar radio flux (f10. 7). *Space Weather*, *11*(7), 394–406. https://doi.org/10.1002/swe.20064
Uriot, T., Izzo, D., Simões, L. F., Abay, R., Einecke, N., Rebhan, S., et al. (2022). Spacecraft collision avoidance challenge: Design and results of a machine learning competition. *Astrodynamics*, *6*(2), 121–140. https://doi.org/10.1007/s42064-021-0101-5
Vallado, D. A. (2001). *Fundamentals of astrodynamics and applications* (Vol. 12). Springer Science and Business Media.
Wang, W., Burns, A., Wiltberger, M., Solomon, S., & Killeen, T. (2008). Altitude variations of the horizontal thermospheric winds during geomagnetic storms. *Journal of Geophysical Research*, *113*(A2). https://doi.org/10.1029/2007ja012374
Zhang, S. P., & Shepherd, G. G. (2000). Neutral winds in the lower thermosphere observed by windii during the april 4–5th, 1993 storm. *Geophysical Research Letters*, *27*(13), 1855–1858. https://doi.org/10.1029/2000gl000034